

Chemical evolution of Red MSX Sources in the southern sky

Naiping Yu¹, Jinlong Xu¹

ABSTRACT

Red MSX Sources(RMSs) are regarded as excellent candidates of massive star-forming regions. In order to characterize the chemical properties of massive star formation, we made a systematic study of 87 RMSs in the southern sky, using archival data taken from the Atacama Pathfinder Experiment (APEX) Telescope Large Area Survey of the Galaxy (ATLASGAL), the Australia Telescope Compact Array (ATCA), and the Millimetre Astronomy Legacy Team Survey at 90 GHz (MALT90). According to previous multi-wavelength observations, our sample could be divided into two groups: massive young stellar objects (MYSOs) and HII regions. Combined with the MALT90 data, we calculated the column densities of N_2H^+ , C_2H , HC_3N and HNC , and found that they are not much different from previous studies made in other massive star-forming regions. However, their abundances are relatively low compared to infrared dark clouds (IRDCs). The abundances of N_2H^+ and HNC in our sample are at least one magnitude lower than those found IRDCs, indicating chemical depletions in the relatively hot gas. Besides, the fractional abundances of N_2H^+ , C_2H and HC_3N seem to decrease as a function of their Lyman continuum fluxes (N_L), indicating these molecules could be destroyed by UV photons when HII regions have formed inside. We also find the C_2H abundance decreases faster than HC_3N with respect to N_L . The abundance of HNC has a tight correlation with that of N_2H^+ , indicating it may be also preferentially formed in cold gas. We regard our RMSs are in a relatively late evolutionary stage of massive star formation.

Subject headings: stars: formation - ISM: abundances - ISM: clouds - ISM: molecules

1. Introduction

The study of massive stars are important to astrophysics. They dominate the luminosity of galaxies. Their feedback to the environment will have a profound effect on the physical

¹National Astronomical Observatories, Chinese Academy of Sciences, Beijing 100012, China

and chemical evolutions of the surrounding interstellar medium (ISM), and even may trigger the next generation of star formation that will take place therein (e.g. Yu et al. 2014). At the end of their short life, they release heavy elements to the cosmic space in the form of supernova explosions, which will have an immense impact to the evolution of galaxies. In the last two decades, a lot of progress has been made both in theories and observations of star formation. However, massive star formation is still poorly understood compared with their low-mass counterparts. One reason is that they are rare and evolve quickly. The other reason is that they used to form in dense clusters at far distances, which makes it hard to study them individually. According to the review made by Zinnecker & Yorke (2007), the processes of a massive star formation could roughly be divided into four different observable stages. The first stage is the prestellar phase that can be found in IRDCs (e.g. Perault et al. 1996; Egan et al. 1998; Peretto & Fuller 2009). The typical temperature of this stage is about 10 K, as no stars have formed inside. The next stage is the “hot core” phase, with various complex organic molecular emissions inside and a typical temperature of ~ 100 K (e.g. Cesaroni et al. 1992; Cesaroni et al. 2010). The third stage is hypercompact and ultracompact HII regions and the final stage is compact and classical HII regions.

It is also important to understand chemical processes that may occur during all stages of massive star formation. In the early stages of massive star formation, the gas is cold and diffuse. Thus the chemistry is dominated by low-temperature gas-phase reactions, leading to the formation of small radicals and unsaturated molecules (e.g. Herbst & Klemperer 1972). During the gas collapse phase, the density of gas becomes so high and the temperature so low that many atoms and molecules are absorbed onto the dust grains, forming various kinds of icy mantles (e.g. Shematovich 2012). Many complex reactions could take place between these mantles. These kind of grain-surface chemical processes are great important to some organic species. For example, both observations and chemical models indicate methanol is mainly formed through grain-surface reactions, as the production of methanol is ineffective by gas-phase reactions (Wirstrom et al. 2011). The dust works as a catalyst in these reactions. In the hot core stage, a massive young stellar object has just formed inside. Its radiations quickly heat up the surrounding gas and dust. Icy mantles on the dust evaporate back into the gas phase. Warm gas-phase chemistry between these fresh material becomes important both in the formation and destruction of many complex organic molecules (e.g. Belloche et al. 2008; Qin et al. 2011). In the HII regions, intense UV radiations are emitted from the central O/B star(s), leading to the destructions and/or productions of many species (e.g. Fuente et al. 1993; Yu & Wang 2015).

In order to study massive star formation, we first need a large sample of massive star-forming candidates. By comparing the colors of MSX and 2MASS point sources to those already known MYSOs, Lumsden et al. (2002; 2013) selected about 2000 MYSO candidates.

This is known as the RMS survey. The RMS survey is still an on-going project. Follow-up infrared and radio observations indicate they are indeed excellent candidates of massive star-forming regions (e.g. Urquhart et al. 2007; Cooper et al. 2013; Yu & Wang 2014). However, chemical properties of RMSs are still less studied. What is the chemistry in RMSs? Are they similar to other massive star-forming regions like IRDCs and/or extended green objects (EGOs)? With the aim to better understand the chemical evolution of massive star formation, we have studied the chemical properties of 87 RMSs and compared them with previous observations of other massive star-forming regions in this paper.

2. Data and Source Selections

Our molecular line data comes from MALT90, which is an international project aims to characterize the sites within our Galaxy where massive star formation will take place (e.g. Foster et al. 2011; Jackson et al. 2013). This project is performed with Mopra, a 22-m single dish radio telescope located near Coonabarabran in New South Wales, Australia. By splitting the Mopra Spectrometer (MOPS) into 16 zoom bands of 138 MHz each, Mopra could map 16 molecular lines simultaneously with a velocity resolution of $\sim 0.11 \text{ km s}^{-1}$ at frequencies near 90 GHz. The critical densities of these molecular lines range from 2×10^5 to $3 \times 10^6 \text{ cm}^{-3}$ (see Table 1 in Rathborne et al. 2014). And these lines will help us to probe the physical, chemical, and evolutionary states of dense high-mass star-forming clumps. The angular resolution of Mopra is $38''$, with a beam efficiency between 0.49 at 86 GHz and 0.42 at 115 GHz (Ladd et al. 2005). The pointing accuracy of the main MALT90 maps is about $8''$ and the absolute flux uncertainty is in the range of $10 \sim 17\%$ depending on the transition in question (Foster et al. 2013). The target clumps of this survey are selected from the 870 micron APEX Telescope Large Area Survey of the Galaxy (ATLASGAL) (Schuller et al. 2009; Contreras et al. 2013), with Galactic longitude range of $\sim -60^\circ$ to $\sim 15^\circ$ and Galactic latitude range of -1° to $+1^\circ$. The MALT90 data are originally stored in RPFITS format. Using software packages of CLASS (Continuum and Line Analysis Single-Disk Software) and GREG (Grenoble Graphic), we conducted the data. The data files are publicly available and can be downloaded from the MALT90 Home Page¹.

Using ATCA, Urquhart et al. (2007) observed radio emissions of 826 RMSs in the southern sky. This programme divided their sources into three groups: MYSO candidates, HII regions and others such as evolved stars and planetary nebulae (PNe). Our sources are selected from this sample. Considering radio interferometers may have difficulty imaging

¹ <http://atoa.atnf.csiro.au/MALT90>

extended emissions in the Galactic plane, we also have checked our sources with the data taken from the Sydney University Molonglo Sky Survey (SUMSS) carried out at 843 MHz with the Molonglo Observatory Synthesis Telescope (MOST) (Mauch et al. 2003). In our sample, sources are regarded as MYSO candidates if no radio emissions have been detected by ATCA and MOST, otherwise they are regarded as HII regions. We should mention here that even though many RMSs are radio-quiet in the observations of ATCA and MOST, they are still regarded as HII region candidates in the Red MSX Source survey database², because their positions in the color-color diagrams (CCD) are consistent with already known HII regions. These sources may be real MYSOs or HII regions that their radio emissions are too weak to be detected. Deeper and higher spacial resolution observations should be carried out in the future to found out whether HII regions have formed inside these sources. In order to make our sample unambiguous, these sources are not involved in our study. Besides, given the large beam size of Mopra, the effective diameter of our RMS clumps given by Contreras et al. (2013) should be larger than $38''$ and far from known bubbles or HII regions. Finally, we found 87 RMSs (28 MYSOs and 59 HII regions) having molecular data in MALT90. Our source selection criteria could be summarized in the followings: (i) Sources should be relatively isolated and be detected by MALT90; (ii) The effective diameter of a RMS clump should be larger than $38''$; (iii) For MYSOs, they should be radio-quiet and have similar near and mid-IR colors to already known MYSOs. (iv) For HII regions, radio emissions should have been detected by ATCA and/or MOST, and have similar near and mid-IR colors to already known HII regions. The basic information of our sources is listed in Table 1.

3. Results

3.1. Dust Temperature and H_2 Column Densities

Dust temperature (T_d) is essential in the study of chemical evolution in star formation regions. When T_d is below ~ 20 K, carbon species like CO and CS can be depleted in the cold gas. Derived from adjusting single-temperature dust emission models to the far-infrared intensity maps measured between 160 and $870 \mu\text{m}$ from the Herschel and APEX sky surveys, Guzmán et al. (2015) recently have calculated the dust temperatures and H_2 column densities for ~ 3000 MALT90 clumps. The FWHM of these data differs from $12''$ to $35''$ (the data from the PACS $70 \mu\text{m}$ band is excluded). To make an adequate comparison, they convolved all images to a spacial resolution of $35''$, which is the lowest resolution given by the $500 \mu\text{m}$ SPIRE instrument. We used these dust temperatures and H_2 column densities

² http://rms.leeds.ac.uk/cgi-bin/public/RMS_DATABASE.cgi

derived by Guzmán et al. (2015) in our study due to the similar beam resolution of Mopra (35'' vs 38''). These values are also listed in Table 1 (column 3 and column 5) and the dust temperature distributions are shown in Fig. 1. The mean dust temperature of our RMSs is 26.4 K. This is consistent with many other observations of MYSOs and HII regions (e.g. Hennemann et al. 2009; Sreenilayam & Fich 2011). However, our values are higher than those found in IRDCs (e.g. Vasyunina et al. 2011; Hoq et al. 2013), indicating our sources are relatively more evolved. From Fig. 1, it can also be noted that in our two subgroups, HII regions are warmer than MYSOs on average. Kolmogorov-Smirnov (K-S) test gives a probability of less than 0.01 % that these two groups originate from the same parent population. Typically, the difference will be regarded as significant when the K-S test gives a percentage lower than 5%. It is reasonable that gas and dust will get warmer as the central star(s) evolves.

Urquhart et al. (2007) have completed the 4.8 and 8.6 GHz observations of 826 RMS sources in the southern sky using observations of ATCA. We use these data to estimate the Lyman continuum fluxes of our HII regions. Assuming an electron temperature of $T_e = 10^4$ K, the number of UV ionizing photons needed to keep an HII region ionized could be given as (Chaisson 1976; Guzmán et al. 2012)

$$N_L = 7.6 \times 10^{46} \left(\frac{S_\nu}{Jy} \right) \left(\frac{D}{kpc} \right)^2 \left(\frac{\nu}{GHz} \right)^{0.1} \left(\frac{T_e}{10^4 K} \right)^{-0.45} s^{-1} \quad (1)$$

where ν is the frequency and S_ν is the integrated flux density given by Urquhart et al. (2007), D is the kinematic distance derived by Urquhart et al. (2008). The large number of Lyman continuum fluxes (listed in Table 1, column 4) indicate that they are probably massive O or early B-type star formation regions.

3.2. Column Densities and Abundances

Assuming local thermodynamic equilibrium (LTE) conditions and a beam filling factor of 1, the column densities of N_2H^+ , C_2H , HC_3N and HNC could be derived from (e.g. Garden et al. 1991; Sanhueza et al. 2012):

$$N = \frac{8\pi\nu^3}{c^3 R} \frac{Q_{rot}}{g_u A_{ul}} \frac{\exp(E_l/kT_{ex})}{1 - \exp(-h\nu/kT_{ex})} \frac{\tau}{1 - \exp(-\tau)} \frac{\int T_{mb} dv}{J(T_{ex}) - J(T_{bg})} \quad (2)$$

where c is the velocity of light in the vacuum, g_u is the statistical weight of the upper level, A_{ul} is the Einstein coefficient for spontaneous transition, E_l is the energy of the lower level, Q_{rot} is the partition function, T_{bg} is the background temperature, τ is the optical depth, T_{ex} is the excitation temperature in all cases. We assume that T_{ex} is equal to the dust temperature

(T_d) derived by Guzmán et al. (2015). R is only relevant for hyperfine transitions because it takes into account the satellite lines correcting by their relative opacities. The value of R is 5/9 for N_2H^+ , 5/12 for C_2H and 1.0 for transitions without hyperfine structure. The values of g_u , A_{ul} and E_l could be found in the Cologne Database for Molecular Spectroscopy (CDMS) (Müller et al. 2001, 2005). $J(T)$ is defined by

$$J(T) = \frac{h\nu}{k} \frac{1}{e^{h\nu/kT} - 1} \quad (3)$$

Near 90 GHz, the N_2H^+ (1-0) line has 15 hyperfine structures (HFS) out of which seven have a different frequency (e.g. Pagani et al. 2009; Keto & Rybicki 2010). In massive star-forming regions, these velocity components tend to blend into three groups because of turbulence (see Fig. 2 of Purcell et al. 2009). We follow the procedure outlined by Purcell et al. (2009) to estimate the optical depth of N_2H^+ . Assuming the line widths of the individual hyperfine components are all equal, the integrated intensities of the three blended groups should be in the ratio of 1:5:3 under optically thin conditions. The optical depth can then be derived from the ratio of the integrated intensities of any two groups using the following equation:

$$\frac{\int T_{MB,1} dv}{\int T_{MB,2} dv} = \frac{1 - \exp(-\tau_1)}{1 - \exp(-a\tau_1)} \quad (4)$$

where a is the expected ratio of τ_2/τ_1 under optically thin conditions. We determined the optical depth only from the intensity ratio of group 1/group 2 (defined by Purcell et al. 2009), as anomalous excitation of the $F_1F = 10-11$ and $12-12$ components (in our group 3) has been reported by Caselli et al. (1995). Here the value of a is 5. To derive the line intensities and peak emissions, we fitted the three groups with three Gaussian profiles from the averaged pixels inside $38''$. The integrated intensities of group 1 and group 2 are listed in table 2 and the derived column densities of N_2H^+ are listed in table 4. Finally, the fractional abundance of N_2H^+ with respect to H_2 could be estimated by $\chi(\text{N}_2\text{H}^+) = \text{N}(\text{N}_2\text{H}^+)/\text{N}(\text{H}_2)$. The derived values are listed in Table 5.

C_2H ($N = 1 - 0$) has six hyperfine components out of which two ($N = 1 - 0, J = 3/2 - 1/2, F = 2 - 1$ and $N = 1 - 0, J = 3/2 - 1/2, F = 1 - 0$) could easily be detected in MALT90. The optical depth of C_2H ($F = 2 - 1$) can be obtained by comparing its hyperfine components. Under the assumption of optically thin, the intensity ratio of C_2H ($F = 2 - 1$) and C_2H ($F = 1 - 0$) should be 2.0 (Tucker et al. 1974). Thus, the opacity of the brightest component of C_2H could be given by

$$\frac{1 - e^{-0.5\tau}}{1 - e^{-\tau}} = \frac{T_{mb}(F = 1 - 0)}{T_{mb}(F = 2 - 1)} \quad (5)$$

The peak intensities of these two components of C_2H are listed in table 3. The column densities of C_2H can be derived through equation 2. The calculated parameters are also listed in table 4.

Many studies indicate HC_3N ($J = 10 - 9$) used to be optically thin (e.g. Chen et al. 2013). In order to compare our study with that of Vasyunina et al. (2011) and Sanhueza et al. (2012), we also assume that this transition is optically thin here. The optical thickness of HNC could be estimated by comparing the intensity of its isotopologue HN^{13}C :

$$\frac{1 - e^{-\tau_{12}}}{1 - e^{-\tau_{12}/X}} = \frac{{}^{12}T_{mb}}{{}^{13}T_{mb}} \quad (6)$$

where $X \sim [{}^{12}\text{C}]/[{}^{13}\text{C}]$ is the isotope abundance ratio. Here we use a constant $X = 50$ in our calculations (Purcell et al. 2006).

4. Analysis and Discussions

4.1. N_2H^+ (*Diazenylium*)

N_2H^+ is one of the most detected molecules in our study. According to previous observations made in low-mass star-forming regions and chemical evolution models, N_2H^+ is mainly destroyed via $\text{N}_2\text{H}^+ + \text{CO} \rightarrow \text{HCO}^+ + \text{N}_2$ when CO evaporates into the gas phase (e.g. Bergin & Langer 1997; Lee et al. 2004). Thus we would expect to find that the N_2H^+ abundance decreases as a function of evolutionary stage. However, this trend was not found in the observations of Sanhueza et al. (2012) and Hoq et al. (2013). They regard this may be caused by their beam dilution, and/or chemical processes of N_2H^+ in massive star-forming regions may be different from those in low-mass star-forming regions. In our study, we find the column densities of N_2H^+ range from $0.31 \times 10^{13} \text{ cm}^{-2}$ to $4.24 \times 10^{13} \text{ cm}^{-2}$, with a mean value of $1.51 \times 10^{13} \text{ cm}^{-2}$. These values are not so much different from those found in other massive star-forming regions like IRDCs and EGOs (see table 6). However, we find our N_2H^+ abundances range from 0.4×10^{-10} to 0.8×10^{-9} , with a mean value of only 0.2×10^{-9} . These values are at least one magnitude lower than those found in IRDCs. This may be because our RMSs are relatively more evolved than IRDCs. Fig.2 shows the histograms of the number distributions of N_2H^+ abundances for our total RMSs, MYSOs and HII regions. K-S test gives a possibility of 49% that the two distributions originate from the same parent population, indicating that they are undistinguishable. We found the fractional abundance of N_2H^+ ($\chi(\text{N}_2\text{H}^+)$) seems to decrease as a function of Lyman continuum fluxes N_L as shown in Fig. 3. This may be caused by that in HII regions, N_2H^+ could be destroyed by recombination with electron : $\text{N}_2\text{H}^+ + \text{e}^- \rightarrow \text{N}_2 + \text{H}$ or $\text{NH} + \text{N}$ (e.g. Dislaire et al.

2012; Vigren et al. 2012; Yu et al. 2015).

4.2. C₂H (*Ethynyl*)

C₂H was first detected by Tucker et al. (1974) in interstellar clouds. However it has not been systematically studied and its evolution routes are still not clear in massive star-forming regions. Through observations of NGC7023, Fuente et al. (1993) suggest C₂H is a good photodissociation region (PDR) tracer. At the boundary layers between ionized and molecular gas, UV photons can produce C₂H by reactions with acetylene (C₂H₂): $C_2H_2 + h\nu \rightarrow C_2H + H$. However, based on the high spacial resolution observations of the Submillimeter Array (SMA) and chemical models, Beuther et al. (2008) suggest C₂H may preferentially exist in the outer part of dense gas clumps, as they found that the distribution of C₂H shows a hole in the hot core. In the cold low-mass star-forming cores of Taurus, Pratap et al. (1997) also found strong C₂H emissions. In the high-mass regime of the prestellar IRDC G028.23-00.19, Sanhueza et al. (2013) interestingly found that C₂H have similar spatial distribution and line widths than NH₂D, suggesting that C₂H can also trace cold gas in IRDCs. Thus, C₂H may trace both early and late stages of star formation. Recently, Li et al. (2012) observed 27 massive star-forming regions with water masers. They found their C₂H optical depth declines when molecular clouds evolve from hypercompact HII regions to classical HII regions. On the other hand, Yu & Wang (2015) found that the [C₂H]/[H¹³CO⁺] relative abundance ratio decreases from MYSOs to HII regions. These studies suggest that C₂H might be used as a chemical clock for molecular clouds. In this study, the abundance of C₂H does not show significant difference in our subgroups of MYSOs and HII regions (see Fig. 4). The K-S test gives a probability of 61% that they may originate from the same parent population. The abundances of C₂H range from 1.4×10^{-9} to 1.96×10^{-8} , with an average value of 0.50×10^{-8} . Our mean value is about 3 to 7 times less than those found by Sanhueza et al. (2012) and Vasyunina et al. (2011), indicating slight depletion of C₂H. Fig. 3 (the middle panel) shows the C₂H fractional abundance plotted as a function of N_L in logarithmic scales. It seems the fractional abundance of C₂H decreases as the number of UV photons increases. One reason may be that in dense molecular gas, nearly all carbon is in the form of CO because CO is chemically stable. However, in HII regions UV photons can photodissociate CO into C and O ($CO + h\nu \rightarrow C + O$). Atom C can further be photoionized into C⁺ ($C + h\nu \rightarrow C^+ + e^-$). The enhanced abundances of O and C⁺ can destroy C₂H through reactions $C_2H + O \rightarrow CO + CH$ and $C_2H + C^+ \rightarrow C_3^+ + H$ (Watt et al. 1988). Deep observations and chemical models should be carried out to verify our speculations.

4.3. HC_3N (*Cyanoacetylene*)

HC_3N traces both cold molecular clouds and hot cores. Previous studies indicate HC_3N is mainly produced through $\text{C}_2\text{H}_2 + \text{CN} \rightarrow \text{HC}_3\text{N} + \text{H}$ (Chapman et al. 2009). It is the most simple example of the cyanopolynes, HC_{2n+1}N . The HC_3N abundances we derived range from 0.4×10^{-10} to 1.6×10^{-10} , with a mean value of 0.9×10^{-10} (see table 6). These values are about 5 times less than previous studies made in IRDCs by Sanhueza et al. (2012) and Vasyunina et al. (2011). Fig.5 also shows the number distributions of the HC_3N abundances for MYSOs and HII regions. No real change is clear. The K-S test gives a probability of 59% that they may originate from the same parent population. The bottom panel of Fig. 3 shows the relationship between $\chi(\text{HC}_3\text{N})$ and N_L . It also indicates that the abundance of HC_3N decreases when increasing UV field. One reason maybe that in the strong UV field of HII regions, the reaction $\text{C}_2\text{H}_2 + h\nu \rightarrow \text{C}_2\text{H} + \text{H}$ dominates instead, leading to the production of HC_3N ineffective. However, if this scenario is true, it means that C_2H_2 tends to form more C_2H over HC_3N . Fig. 6 shows the $[\text{C}_2\text{H}]/[\text{HC}_3\text{N}]$ relative abundance ratios plotted as a function of N_L in logarithmic scales. It can be noted that the HC_3N abundance does not decrease faster than C_2H with respect to N_L . There must be another scenario for the destruction of HC_3N in HII regions. More deep observations and chemical models should be carried out to find this scenario.

4.4. HNC and HN^{13}C (*Hydrogen Isocyanide*)

HNC and its isotopologue HN^{13}C are prevalent in cold gas (e.g. Bergin & Tafalla 2007). Hirota et al. (1998) found abundances of HNC in OMC-1 are 1 ~ 2 orders of magnitude less than those in dark cloud cores, indicating destruction of HNC in hot regions. Sanhueza et al (2012) also found the $\text{N}_2\text{H}^+/\text{HNC}$ abundance ratio slightly decrease as IRDCs evolve (see their Fig. 17), suggesting HNC may be preferentially formed in cold gas. In our study, we found the HN^{13}C detection rate in MYSOs is about 2 times higher than in HII regions (39% vs 20%). The HNC abundances we derived in our all RMSs range from 0.5×10^{-9} to 5.6×10^{-9} , with a mean value of 0.2×10^{-8} . This mean value is about 20 times lower than those found in IRDCs by Sanhueza et al. (2012), which would be consistent with HNC being preferentially formed in the cold gas. Although our mean value is similar to that of Vasyunina et al. (2011), we should mention that in their study, Vasyunina et al. (2011) made an assumption that the emission of HNC is optically thin. This assumption will make column densities at least one order of magnitude lower. We also find a tight correlation between $\chi(\text{N}_2\text{H}^+)$ and $\chi(\text{HNC})$ (Fig. 7). The functional form of the linear fit is:

$$\chi(\text{HNC}) = 1.44 \times \chi(\text{N}_2\text{H}^+) \quad (7)$$

with a correlation coefficient $r = 0.74$. Our study also support HNC and HN^{13}C are dense cold tracers.

4.5. Why undistinguishable ?

RMSs are regarded as excellent candidates of massive star-forming regions. Multiwavelength observations have been carried out to study their physical parameters. However their chemical properties are less studied. In this paper, we selected 87 RMSs to study their chemical properties. We found the column densities of N_2H^+ , C_2H , HC_3N and HNC are not much different from previous observations made in IRDCs and EGOs. However, their abundances are relatively low, indicating depletions of them in the late stages of massive star formation, especially those of N_2H^+ and HNC. The value of χ (N_2H^+) and χ (HNC) in our sample are at least one magnitude lower than those found in IRDCs. This may be because that our RMSs are relatively more evolved. In our two subgroups of MYSOs and HII regions, K-S tests suggest that the differences of their chemical properties are not significant. Two reasons may be responsible for this. Firstly, the angular resolution of our MALT90 data is not high enough. At 2.9 kpc, the $38''$ beam dilution corresponds to over half a parsec. Therefore, MALT90 probes not only star-forming cores, but also diffuse envelopes around. Secondly, our source selections are mainly based on the work of Lumsden et al. (2002; 2013) and Urquhart et al. (2007). On the other hand, our sources are also involved in the work of Guzmán et al. (2015). By combining other sky survey data taken with the *Herschel* and *Spitzer* telescope, Guzmán et al. (2015) divided their sample into “Quiescent”, “Protostellar”, “HII region” and “Photodissociation region (PDR)” clumps. 83% (49 in 59) of our HII regions are consistent with their classifications. This means that our source selection criteria for HII regions are reliable. However, according to their classification, our 28 MYSOs involves 19 protostellar and 9 HII regions. Even though all of our MYSO candidates are radio-quiet and have similar infrared colors to already known MYSOs, most of them also show bright emissions at $8\text{ }\mu\text{m}$. This suggests that our MYSO candidates are probably in the late stages of protostellar and HII regions may form inside in the near future.

5. Conclusions

We have studied chemical properties of 87 RMSs in the southern sky, using archival data taken from APEX, ATCA, and Mopra. According to previous multiwavelength observations, we divide our sample into two groups: MYSOs and HII regions. We find the column densities of N_2H^+ , C_2H , HC_3N and HNC are not much different from previous studies made in other

massive star-forming regions. However, their abundances are relatively low compared to IRDCs. The abundances of N_2H^+ and HNC in our sample are at least one magnitude lower than those found IRDCs, indicating chemical depletions in the relatively hot gas. The fractional abundances of N_2H^+ , C_2H and HC_3N seem to decrease as a function of their Lyman continuum fluxes, indicating these molecules could be destroyed when HII regions have formed. Besides, the C_2H abundance seems to decrease faster than HC_3N in HII regions. The abundance of HNC has a tight correlation with that of N_2H^+ , indicating it may be also preferentially formed in cold gas. We regard our RMSs are in a relatively late evolutionary stage of massive star formation.

6. ACKNOWLEDGEMENTS

We thank the referee for detailed comments which have considerably improved this paper. This paper has made use of information from the Red MSX Source survey database http://rms.leeds.ac.uk/cgi-bin/public/RMS_DATABASE.cgi and the ATLASGAL Database Server http://atlasgal.mpifr-bonn.mpg.de/cgi-bin/ATLASGAL_DATABASE.cgi. The Red MSX Source survey was constructed with support from the Science and Technology Facilities Council of the UK. The ATLASGAL project is a collaboration between the Max-Planck-Gesellschaft, the European Southern Observatory (ESO) and the Universidad de Chile. This research made use of data products from the Millimetre Astronomy Legacy Team 90 GHz (MALT90) survey. The Mopra telescope is part of the Australia Telescope and is funded by the Commonwealth of Australia for operation as National Facility managed by CSIRO. This paper is supported by National Natural Science Foundation of China under grants of 11503037.

REFERENCES

- Belloche, A., Menten, K. M., Comito, C., et al. 2008, *A&A*, 482, 179
- Bergin, E. A., & Langer, W. D. 1997, *ApJ*, 486, 316
- Bergin, E. A., & Tafalla, M. 2007, *ARA&A*, 45, 339
- Beuther, H., Semenov, D., Henning, T., & Linz, H. 2008, *ApJ*, 675, L33
- Casoli, F., Combes, F., Dupraz, C., Gerin, M., & Boulanger, F. 1986, *A&A*, 169, 281
- Cesaroni, R., Hofner, P., Araya, E., & Kurtz, S. 2010, *A&A*, 509, 50

- Cesaroni, R., Walmsley, C. M., & Churchwell, E. 1992, *A&A*, 256, 618
- Chaisson, E. J., 1976, in Avrett E. H., ed., *Frontiers of Astrophysics*. Harvard Univ. Press, Harvard, p. 259
- Chapman, J. F., Millar, T. J., Wardle, M., Burton, M. G., & Walsh, A. J. 2009, *MNRAS*, 394, 221
- Chen, X., Gan, C.G., Ellingsen, S., et al. 2013, *ApJS*, 206, 22
- Contreras, Y., Schuller, F., Urquhart, J. S., et al. 2013, *A&A*, 549, A45
- Daniel, F., Cernicharo, J., & Dubernet, M.-L. 2006, *ApJ*, 648, 461
- Dislaire, V., Hily-Blant, P., Faure, A., et al. 2012, *A&A*, 537, 20A
- Egan, M. P., Shipman, R. F., Price, S. D., et al. 1998, *ApJ*, 494, 199
- Foster, J. B., Jackson, J. M., Barnes, P. J., et al. 2011, *ApJS*, 197, 25
- Foster, J. B., Rathborne, J. M., Sanhueza, P., et al. 2013, *PASA*, 30, 38
- Fuente, A., Martin-Pintado, J., Cernicharo, J., & Bachiller, R. 1993, *A&A*, 276, 473
- Guzmán, A., Garay, G., Brooks, K. J., & Voronkov, M. A. 2012, *ApJ*, 753, 51
- Guzmán, A., Sanhueza, P., Contreras, Y., et al. 2015, *ApJ*, 815, 130
- Hennemann, M., Birkmann, S. M., Krause, O., et al. 2009, *ApJ*, 693, 1379
- Henning, T., Pfau, W., & Altenhoff, W. J. 1990, *A&A*, 227, 542
- Herbst, E., & Klemperer, W. 1972, *ApJ*, 185, 505
- Hirota, T., Yamamoto, S., Mikami, H., & Ohishi, M. 1998, *ApJ*, 503, 717
- Hoq, S., Jackson, J.M., Foster, J.B., et al. 2013, *ApJ*, 777, 157
- Jackson, J. M., Rathborne, J. M., Foster, J. B., et al. 2013, *PASA*, 30, 57
- Kauffmann, J., Bertoldi, F., Bourke, T. L., Evans, N. J., II, & Lee, C. W. 2008, *A&A*, 487, 993
- Keto, E., & Rybicki, G. 2010, *ApJ*, 716, 1315
- Ladd, N., Purcell, C., Wong, T., & Robertson, S. 2005, *Publ. Astron. Soc. Aust.*, 22, 62

- Lee, J. E., Bergin, E. A., & Evans, N. J. 2004, *ApJ*, 617, 360
- Li, J., Wang, J. Z., Gu, Q. S., Zhang, Z. Y., & Zheng, X. W. 2012, *ApJ*, 745, 47
- Lumsden, S. L., Hoare, M. G., Urquhart, J. S. et al. 2013, *ApJS*, 208, 11.
- Lumsden, S. L., Hoare, M. G., Oudmaijer, R. D., & Richards, D. 2002, *MNRAS*, 336, 621.
- Mauch, T., Murphy, T., Buttery, H. J., et al. 2003, *MNRAS*, 342, 1117
- Müller, H. S. P., Thorwirth, S., Roth, D. A., & Winnewisser, G. 2001, *A&A*, 370, L49
- Müller, H. S. P., Schlöder, F., Stutzki, J., & Winnewisser, G. 2005, *J. Molec. Struct.*, 742, 215
- Ossenkopf, V., & Henning, T. 1994, *A&A*, 291, 943
- Pagani, L., Daniel, F., & Dubernet, M.-L. 2009, *A&A*, 494, 719
- Perault, M., Omont, A., Simon, G., et al. 1996, *A&A*, 315, 165
- Peretto, N., & Fuller, G. A. 2009, *VizieR Online Data Catalog*, 350, 50405
- Pratap, P., Dickens, J. E., Snell, R L., et al. 1997, *ApJ*, 486, 862
- Purcell, C. R., Balasubramanyam, R., Burton, M.G. et al. 2006, *MNRAS*, 367, 553
- Purcell, C. R., Longmore, S. N., Burton, M. G., et al. 2009, *MNRAS*, 394, 323
- Qin, S. L., Schilke, P., Rolffs, R., et al. 2011, *A&A*, 530, L9
- Rathborne, J. M., Longmore, S. N., Jackson, J. M., et al. 2014, *ApJ*, 786, 140
- Sakai, T., Sakai, N., Hirota, T., & Yamaguchi, N. 2010, *ApJ*, 714, 1658
- Sanhueza, P., Jackson, J. M., Foster, J. B., et al. 2012, *ApJ*, 756, 60
- Sanhueza, P., Jackson, J. M., Foster, J. B., et al. 2013, *ApJ*, 773, 123
- Schuller F., Menten K. M., Contreras Y., Wyrowski F., Schilke P., Bronfman L., Henning T., et al. 2009, *A&A*, 504, 415
- Shematovich, V. I. 2012, *SoSyR*, 46, 391s
- Sreenilayam, G., & Fich, M. 2011, *AJ*, 142, 4
- Tucker, K. D., Kutner, M. L., & Thaddeus, P. 1974, *ApJ*, 193, L115

- Urquhart, J. S., Busfield, A. L., Hoare, M. G., et al. 2007, *A&A*, 461, 11
- Urquhart, J. S., Busfield, A. L., Hoare, M. G., et al. 2008 *A&A*, 487, 253
- Vasyunina, T., Linz, H., Henning, Th., et al. 2011, *A&A*, 527, A88
- Vigren, E., Zhaunerchyk, V., Hamberg, M., et al. 2012, *ApJ*, 757, 34
- Yu, N. P., & Wang, J. J. 2014, *MNRAS*, 440, 1213
- Yu, N. P., Wang, J. J., & Li, N. 2014, *MNRAS*, 445, 3374
- Yu, N. P., & Wang, J. J. 2015, *MNRAS*, 451, 2507
- Yu, N. P., Wang, J. J., & Li, N. 2015, *MNRAS*, 446, 2566
- Watt, G. D., White, G. J., Millar, T. J., & van Ardenne, A. 1988, *A&A*, 195, 257
- Williams, J. P., & Cieza, L. A. 2011, *ARA&A*, 49, 67
- Wirstrom, E. S., Geppert, W. D., Hjalmarson, A., et al. 2011, *Observational Tests of Interstellar Methanol Formation*, *Astron. Astrophys.*, vol. 533, p. A24
- Wu, L., Evans, N. J. II, Gao, Y., et al. 2005, *ApJL*, 635, 173
- Wu, L., Evans, N. J. II, Shirley, Y.L., & Knez, C. 2010, *ApJS*, 188, 313
- Zinnecher, H., & Yorke, H. W. 2007, *ARA&A*, 45, 481

Table 1. List of our sources.

RMS name	D^a (kpc)	T_d^b (K)	$\log(N_L)$ (S^{-1})	$N(H_2)^b$ ($\times 10^{22} \text{ cm}^{-2}$)
HII regions				
G300.5047-00.1745	8.9	27.2 (0.7)	...	7.85 (0.36)
G301.1364-00.2249	4.3	29.0 (1.0)	47.31	44.12 (3.09)
G301.8147+00.7808	4.4	29.0 (3.0)	46.30	3.12 (0.37)
G302.0319-00.0613	4.5	34.0 (1.0)	...	4.51 (0.32)
G302.4867-00.0308	4.5	27.0 (4.0)	46.12	4.41 (0.61)
G307.5606-00.5871	7.4	27.1 (0.7)	...	13.32 (0.62)
G307.6138-00.2559	7.0	29.0 (1.0)	...	5.68 (0.40)
G309.9206+00.4790	5.4	33.0 (2.0)	47.40	12.43 (1.11)
G310.1420+00.7583	5.4	29.0 (1.0)	...	10.34 (0.72)
G311.6264+00.2897	7.3	31.0 (1.0)	47.40	13.63 (0.95)
G316.1386-00.5009	7.7	27.0 (1.0)	...	7.32 (0.51)
G317.4298-00.5612	14.2	34.0 (2.0)	46.65	3.93 (0.35)
G318.9148-00.1647	11.0	34.0 (2.0)	48.73	6.68 (0.80)
G320.7779+00.2412	12.3	25.0 (2.0)	46.72	3.50 (0.42)
G321.7209+01.1711	2.8	27.0 (3.0)	...	11.08 (1.32)
G323.4468+00.0968	4.1	24.0 (0.6)	...	4.95 (0.35)
G324.1997+00.1192	6.8	36.0 (2.0)	48.32	15.65 (1.40)
G326.4477-00.7485	4.0	24.0 (1.0)	45.41	7.67 (0.54)
G326.4719-00.3777	3.4	28.0 (1.0)	47.02	10.83 (0.76)
G326.7249+00.6159	1.8	31.0 (1.0)	47.09	15.65 (1.10)
G328.3067+00.4308	5.1	40.0 (1.0)	...	13.32 (0.93)
G328.8074+00.6324	2.8	25.0 (2.0)	...	58.16 (5.23)
G328.9580+00.5671	7.2	26.0 (1.0)	45.51	7.15 (0.50)
G329.3371+00.1469	7.2	38.0 (1.0)	...	12.43 (0.87)
G329.4055-00.4574	4.3	27.0 (2.0)	...	14.95 (1.79)
G329.4211-00.1631	4.5	25.0 (2.0)	...	6.68 (0.60)
G329.4761+00.8414	4.8	30.0 (0.8)	46.77	3.05 (0.14)
G329.8145+00.1411	4.9	23.0 (0.6)	45.27	6.83 (0.48)
G330.2845+00.4933	5.3	25.0 (1.0)	46.40	4.73 (0.33)
G330.2935-00.3946	10.0	32.0 (1.0)	48.18	10.83 (0.76)
G330.8845-00.3721	3.8	28.0 (1.0)	47.22	39.32 (2.75)
G330.9544-00.1817	9.6	37.0 (1.0)	48.63	66.77 (4.67)
G331.1282-00.2436	4.9	24.4 (0.6)	...	31.96 (1.50)
G331.4181-00.3546	3.9	23.0 (5.0)	46.54	9.22 (0.81)
G331.5582-00.1206	5.5	26.1 (0.8)	...	18.82 (1.32)

Table 1—Continued

RMS name	D^a (kpc)	T_d^b (K)	$\log(N_L)$ (S^{-1})	$N(H_2)^b$ ($\times 10^{22} \text{ cm}^{-2}$)
G332.1544-00.4487	3.6	37.2 (0.8)	...	7.49 (0.35)
G332.2944-00.0962	3.6	24.0 (2.0)	46.56	17.56 (1.58)
G332.8256-00.5498	3.6	30.0 (3.0)	47.84	60.90 (7.30)
G333.0299-00.0645	3.6	29.0 (3.0)	...	4.62 (0.64)
G333.0494+00.0324	3.6	27.0 (2.0)	...	3.84 (0.34)
G333.1642-00.0994	5.1	27.0 (2.0)	...	4.95 (0.59)
G336.3684-00.0033	7.7	23.0 (1.0)	47.96	15.65 (1.10)
G337.0047+00.3226	11.4	26.0 (3.0)	47.93	5.18 (0.62)
G337.4050-00.4071	3.1	27.5 (0.7)	46.53	38.42 (1.80)
G337.8442-00.3748	3.0	29.9 (0.9)	45.77	6.23 (0.44)
G337.9947+00.0770	7.8	25.7 (0.7)	...	5.82 (0.41)
G338.0715+00.0126	3.0	25.8 (0.9)	...	16.77 (1.17)
G339.1052+00.1490	4.7	25.0 (1.0)	46.38	4.73 (0.33)
G340.0708+00.9267	4.6	26.0 (2.0)	46.73	5.95 (0.53)
G340.2480-00.3725	3.7	22.0 (1.0)	46.75	14.28 (1.00)
G342.7057+00.1260	3.4	25.2 (0.7)	45.18	15.30 (1.07)
G344.4257+00.0451	4.7	30.9 (0.8)	47.20	8.60 (0.60)
G345.0034-00.2240	2.8	25.8 (11.0)	...	41.17 (10.29)
G345.4881+00.3148	2.1	28.0 (1.0)	47.41	35.86 (2.51)
G345.6495+00.0084	14.8	35.0 (0.6)	49.09	11.34 (0.79)
G346.0774-00.0562	10.9	24.0 (4.0)	46.70	6.09 (0.85)
G346.5235+00.0839	11.2	29.0 (2.0)	47.73	4.41 (0.52)
G347.8707+00.0146	3.4	26.0 (1.0)	46.84	7.32 (0.65)
G348.8922-00.1787	11.2	30.0 (2.0)	...	5.55 (0.49)
MYSOs				
G305.2017+00.2072	4.0	26.8 (0.8)	...	31.96(2.24)
G310.0135+00.3892	3.2	28.0 (1.0)	...	8.21 (0.58)
G313.7654-00.8620	7.8	23.0 (2.0)	...	11.87(1.06)
G314.3197+00.1125	3.6	22.0 (1.0)	...	7.15 (0.50)
G318.9480-00.1969	2.4	25.6 (0.4)	...	17.16(1.20)
G320.2437-00.5619	9.5	18.0 (2.0)	...	5.95 (0.53)
G326.4755+00.6947	1.8	22.3 (0.6)	...	38.42(2.69)
G326.5437+00.1684	4.4	19.0 (4.0)	...	10.11(1.70)
G327.1192+00.5103	4.9	27.0 (1.0)	...	7.85 (0.55)
G329.0663-00.3081	11.6	18.5 (0.6)	...	13.02(0.91)

Table 1—Continued

RMS name	D^a (kpc)	T_d^b (K)	$\log(N_L)$ (S^{-1})	$N(H_2)^b$ ($\times 10^{22} \text{ cm}^{-2}$)
G330.9288-00.4070	11.9	20.5 (0.5)	...	9.22 (0.65)
G332.4683-00.5228	3.6	21.0 (1.0)	...	9.22 (0.65)
G332.9636-00.6800	3.2	22.0 (1.0)	...	21.61(1.51)
G333.3151+00.1053	3.6	23.0 (1.0)	...	9.43 (0.84)
G333.3752-00.2015	3.6	23.0 (2.0)	...	4.73 (0.42)
G335.0611-00.4261	2.8	22.5 (1.0)	...	14.28(1.00)
G337.1555-00.3951	3.1	17.6 (0.5)	...	6.68 (0.47)
G338.2801+00.5419	4.1	20.8 (0.8)	...	7.15 (0.50)
G338.9196+00.5495	4.2	20.0 (1.0)	...	58.16(4.07)
G339.6221-00.1209	2.8	25.6 (1.0)	...	7.67 (0.54)
G341.1281-00.3466	3.3	23.3 (0.4)	...	6.83 (0.48)
G341.2182-00.2136	3.4	23.7 (0.6)	...	12.72(0.59)
G342.9583-00.3180	12.7	21.2 (0.5)	...	3.42 (0.16)
G343.5213-00.5171	3.2	20.0 (2.0)	...	6.53 (0.78)
G345.2619-00.4188	2.7	19.9 (0.5)	...	4.62 (0.21)
G345.7172+00.8166	1.6	20.0 (1.0)	...	11.60(0.81)
G346.4809+00.1320	15.0	23.0 (2.0)	...	2.91 (0.34)
G348.6491+00.0225	11.1	21.0 (1.0)	...	4.95 (0.44)

^aUrquhart et al. (2008).

^bThese values are from Guzmán et al. (2015).

Table 2. Integrated intensities of N_2H^+ , C_2H , HC_3N , HN^{13}C .

RMS name	N_2H^+ Group1 (K km s ⁻¹)	N_2H^+ Group2 (K km s ⁻¹)	C_2H F = 2 - 1 (K km s ⁻¹)	HC_3N J = 10 - 9 (K km s ⁻¹)	HN^{13}C J = 1 - 0 (K km s ⁻¹)	HNC J = 1 - 0 (K km s ⁻¹)
HII regions						
G300.5047-00.1745	2.53 (0.26)	4.43 (0.22)
G301.1364-00.2249	1.23(0.21)	3.22 (0.20)	6.31 (0.18)	4.37 (0.17)	...	12.23 (0.17)
G301.8147+00.7808	...	1.67 (0.14)	1.52 (0.16)	3.26 (0.13)
G302.0319-00.0613	3.37 (0.36)	4.19 (0.32)
G302.4867-00.0308	3.70 (0.23)
G307.5606-00.5871	1.27(0.20)	7.87 (0.34)	2.14 (0.21)	2.08 (0.19)	...	9.33 (0.24)
G307.6138-00.2559	1.51(0.23)	3.15 (0.20)	4.83 (0.20)	7.33 (0.17)
G309.9206+00.4790	9.83 (0.66)
G310.1420+00.7583	1.04(0.13)	4.27 (0.17)	2.73 (0.18)	2.57 (0.21)	...	9.28 (0.20)
G311.6264+00.2897
G316.1386-00.5009	1.23(0.13)	5.45 (0.15)	3.67 (0.17)	1.41 (0.13)	...	8.01 (0.18)
G317.4298-00.5612	1.60 (0.17)
G318.9148-00.1647	0.97 (0.16)	...	7.73 (0.54)
G320.7779+00.2412	...	1.52 (0.19)	1.51 (0.19)
G321.7209+01.1711	1.47(0.16)	5.78 (0.21)	3.56 (0.20)	1.64 (0.19)	...	7.74 (1.81)
G323.4468+00.0968	1.15(0.20)	4.78 (0.17)	5.92 (0.20)
G324.1997+00.1192	2.82 (0.20)	10.41 (0.25)
G326.4477-00.7485	1.69(0.19)	6.79 (0.18)	...	1.77 (0.17)	...	4.55 (0.21)
G326.4719-00.3777	1.74(0.17)	6.64 (0.20)	4.41 (0.22)	1.97 (0.15)	...	8.90 (0.18)
G326.7249+00.6159	2.02(0.18)	9.74 (0.21)	4.9 (0.25)	3.30 (0.22)	...	17.34 (0.24)
G328.3067+00.4308	6.15 (0.24)	2.09 (0.19)	...	18.22 (0.88)
G328.8074+00.6324	1.80(0.15)	7.32 (0.17)	4.85 (0.17)	7.92 (0.21)	2.43 (0.18)	14.92 (0.19)
G328.9580+00.5671	0.96(0.13)	5.09 (0.19)	4.17 (0.21)	1.82 (0.15)	...	6.71 (0.18)
G329.3371+00.1469	0.95(0.18)	5.52 (0.26)	5.09 (0.22)	3.4 (0.16)	1.13 (0.16)	20.92 (0.25)
G329.4055-00.4574	1.98(0.18)	6.27 (0.57)	4.51 (0.19)	4.12 (0.16)	1.41 (0.21)	8.64 (0.36)
G329.4211-00.1631	1.80(0.15)	8.01 (0.17)	2.48 (0.18)	1.37 (0.15)	...	9.65 (0.17)
G329.4761+00.8414	0.50(0.15)	1.78 (0.18)	4.20 (0.19)
G329.8145+00.1411	1.55(0.22)	6.19 (0.29)	5.96 (0.26)
G330.2845+00.4933	0.52(0.09)	3.26 (0.18)	4.88 (0.21)
G330.2935-00.3946	2.76 (0.19)	9.72 (0.21)
G330.8845-00.3721	2.09(0.23)	7.21 (0.24)	8.24 (0.22)	6.4 (0.21)	1.76 (0.19)	18.61 (0.22)
G330.9544-00.1817	6.11 (0.24)	8.11 (0.26)	2.52 (0.25)	24.85 (2.10)
G331.1282-00.2436	2.45(0.20)	12.57(0.32)	4.07 (0.23)	4.75 (0.21)	...	13.68 (0.93)
G331.4181-00.3546	2.29(0.33)	7.78 (0.35)	6.99 (0.38)

Table 2—Continued

RMS name	N ₂ H ⁺ Group1 (K km s ⁻¹)	N ₂ H ⁺ Group2 (K km s ⁻¹)	C ₂ H F = 2 - 1 (K km s ⁻¹)	HC ₃ N J = 10 - 9 (K km s ⁻¹)	HN ¹³ C J = 1 - 0 (K km s ⁻¹)	HNC J = 1 - 0 (K km s ⁻¹)
G331.5582-00.1206	1.81(0.15)	7.59 (0.18)	...	2.27 (0.19)	...	5.58 (0.17)
G332.1544-00.4487	5.85 (0.26)	10.40 (0.12)
G332.2944-00.0962	2.20(0.12)	9.11 (0.15)	4.25 (0.18)	2.52 (0.16)	...	9.19 (0.18)
G332.8256-00.5498	3.52(0.11)	17.28(1.06)	10.37(0.28)	9.80 (0.22)	3.5 (0.23)	29.73 (0.25)
G333.0299-00.0645	0.49(0.10)	2.42 (0.12)	3.28 (0.16)	1.62 (0.12)	...	4.25 (0.14)
G333.0494+00.0324	0.43(0.09)	2.32 (0.11)	2.30 (0.16)	4.97 (0.14)
G333.1642-00.0994	2.67(0.28)	4.97 (0.30)	4.69 (0.61)
G336.3684-00.0033	3.16 (0.30)	16.38 (0.31)
G337.0047+00.3226	0.39(0.12)	3.37 (0.22)	4.81 (0.18)
G337.4050-00.4071	2.51(0.17)	10.53(0.17)	6.75 (0.19)	7.31 (0.17)	2.08 (0.17)	21.05 (0.18)
G337.8442-00.3748	0.78(0.15)	5.16 (0.15)	2.74 (0.19)	1.69 (0.12)	...	7.28 (0.14)
G337.9947+00.0770	3.02 (0.17)	9.27 (0.17)
G338.0715+00.0126
G339.1052+00.1490	0.94(0.10)	5.02 (0.14)	5.99 (0.15)
G340.0708+00.9267	1.37(0.16)	6.21 (0.23)	3.16 (0.18)	1.75 (0.15)	...	8.97 (0.17)
G340.2480-00.3725	5.02(0.13)	23.22(0.18)	4.31 (0.20)	5.70 (0.16)	3.11 (0.16)	18.87 (0.82)
G342.7057+00.1260	3.45(0.19)	16.00(0.29)	6.42 (0.22)	5.84 (0.18)	2.05 (0.17)	15.52 (0.57)
G344.4257+00.0451	1.56(0.13)	7.08 (0.16)	3.94 (0.23)	2.54 (0.13)	1.51 (0.16)	9.48 (0.18)
G345.0034-00.2240	3.89(0.16)	11.77(0.42)	3.54 (0.23)	10.46(0.27)	3.23 (0.23)	12.33 (0.56)
G345.4881+00.3148	3.27(0.24)	15.17(0.53)	11.53(0.30)	9.27 (0.31)	3.17 (0.28)	35.97 (0.56)
G345.6495+00.0084	5.19 (0.32)
G346.0774-00.0562	1.88(0.21)	6.85 (0.26)	5.05 (0.27)
G346.5235+00.0839	3.48 (0.18)
G347.8707+00.0146	2.95 (0.20)	9.48 (0.24)
G348.8922-00.1787	...	2.52 (0.16)	1.91 (0.19)	6.36 (0.19)

MYSOs

G305.2017+00.2072	6.90 (0.26)	7.74 (0.27)	...	21.23 (0.27)
G310.0135+00.3892	1.56(0.13)	5.32 (0.14)	2.81 (0.14)	1.73 (0.13)	...	6.02 (0.13)
G313.7654-00.8620	3.18(0.16)	15.75(0.22)	4.07 (0.24)	3.86 (0.22)	1.66 (0.17)	16.38 (0.21)
G314.3197+00.1125	1.45(0.15)	7.28 (0.20)	...	1.20 (0.17)	...	3.76 (0.27)
G318.9480-00.1969	3.06(0.13)	13.59(0.15)	3.25 (0.18)	4.19 (0.17)	1.78 (0.19)	17.42 (2.38)
G320.2437-00.5619	0.60(0.13)	2.92 (0.18)	2.01 (0.17)
G326.4755+00.6947	4.08(0.21)	17.31(0.25)	5.06 (0.28)	4.81 (0.24)	1.66 (0.19)	19.31 (1.48)
G326.5437+00.1684	1.30(0.21)	7.13 (0.30)	1.83 (1.26)	7.59 (0.30)

Table 2—Continued

RMS	N ₂ H ⁺	N ₂ H ⁺	C ₂ H	HC ₃ N	HN ¹³ C	HNC
name	Group1	Group2	F = 2 - 1	J = 10 - 9	J = 1 - 0	J = 1 - 0
	(K km s ⁻¹)	(K km s ⁻¹)	(K km s ⁻¹)	(K km s ⁻¹)	(K km s ⁻¹)	(K km s ⁻¹)
G327.1192+00.5103	0.64(0.14)	3.69 (0.19)	2.03 (0.26)	3.04 (0.26)
G329.0663-00.3081	2.72(0.16)	13.58(0.29)	2.65 (0.21)	4.23 (0.21)	2.61 (0.21)	11.10 (0.21)
G330.9288-00.4070	1.44(0.11)	5.72 (0.14)	1.53 (0.14)	1.20 (0.16)	0.95 (0.14)	5.95 (0.14)
G332.4683-00.5228	1.88(0.13)	11.23(0.17)	4.16 (0.21)	3.76 (0.19)	1.66 (0.17)	13.63 (0.25)
G332.9636-00.6800	4.12(0.32)	12.80(0.66)	5.69 (0.32)	4.87 (0.32)	...	14.55 (0.46)
G333.3151+00.1053	2.68(0.17)	13.25(0.21)	3.40 (0.30)	3.20 (0.22)	1.2 (0.23)	14.48 (0.26)
G333.3752-00.2015	0.44(0.14)	2.31 (0.26)	3.57 (0.26)
G335.0611-00.4261	2.12(0.26)	9.05 (0.30)	7.46 (0.46)
G337.1555-00.3951
G338.2801+00.5419	1.59(0.19)	8.91 (0.22)	11.35 (0.53)
G338.9196+00.5495	8.87(0.26)	40.16(0.46)	6.73 (0.29)	8.34 (0.26)	4.19 (0.27)	25.37 (0.87)
G339.6221-00.1209	1.69(0.14)	9.72 (0.16)	3.47 (0.30)	2.41 (0.17)	1.84 (0.24)	12.65 (0.62)
G341.1281-00.3466	0.90(0.22)	5.04 (0.23)	7.94 (0.24)
G341.2182-00.2136	2.91(0.23)	14.41(0.26)	3.04 (0.11)	2.97 (0.25)	...	9.42 (0.31)
G342.9583-00.3180	1.12(0.20)	4.25 (0.25)	4.05 (0.25)
G343.5213-00.5171	1.98(0.12)	9.38 (0.14)	...	1.18 (0.10)	...	6.32 (0.16)
G345.2619-00.4188	1.30(0.19)	3.33 (0.16)	1.45 (0.17)	0.81 (0.13)	...	3.74 (0.20)
G345.7172+00.8166	2.99(0.13)	11.18(0.16)	2.84 (0.16)	2.74 (0.14)	1.6 (0.15)	8.95 (0.36)
G346.4809+00.1320	...	1.82 (0.19)	3.69 (0.62)
G348.6491+00.0225	1.70(0.18)	2.94 (0.25)	6.95 (0.21)

Table 3. Peak intensities of N_2H^+ , C_2H , HC_3N , HN^{13}C .

RMS name	N_2H^+ Group2 (K)	C_2H F = 1 - 0 (K)	C_2H F = 2 - 1 (K)	HC_3N J = 10 - 9 (K)	HN^{13}C J = 1 - 0 (K)	HNC J = 1 - 0 (K)
HII regions						
G300.5047-00.1745	0.25	0.21	0.47	1.03
G301.1364-00.2249	0.79	0.85	1.46	0.96	...	2.75
G301.8147+00.7808	0.79	0.25	0.61	1.41
G302.0319-00.0613	1.03	1.46
G302.4867-00.0308	0.98
G307.5606-00.5871	1.36	0.25	0.39	0.46	...	1.66
G307.6138-00.2559	0.89	0.57	1.32	2.00
G309.9206+00.4790	1.56
G310.1420+00.7583	1.28	0.38	0.93	0.69	...	2.36
G311.6264+00.2897
G316.1386-00.5009	1.68	0.68	1.01	0.55	...	1.83
G317.4298-00.5612	0.46
G318.9148-00.1647	0.30	...	1.03
G320.7779+00.2412	0.51	0.87
G321.7209+01.1711	1.47	0.67	1.23	0.59	...	1.89
G323.4468+00.0968	1.91	1.72
G324.1997+00.1192	...	0.28	0.62	1.70
G326.4477-00.7485	1.88	0.46	...	0.93
G326.4719-00.3777	2.00	0.54	1.06	0.76	...	2.12
G326.7249+00.6159	2.70	0.64	1.30	0.82	...	4.05
G328.3067+00.4308	...	0.61	0.94	0.43	...	1.18
G328.8074+00.6324	2.24	1.05	1.59	1.91	0.69	4.69
G328.9580+00.5671	1.35	0.50	0.90	0.63	...	1.52
G329.3371+00.1469	1.45	0.52	0.97	0.83	0.37	4.01
G329.4055-00.4574	1.64	0.48	0.90	1.00	0.32	1.71
G329.4211-00.1631	2.72	0.34	1.00	0.62	...	2.72
G329.4761+00.8414	0.60	1.09
G329.8145+00.1411	1.55	1.55
G330.2845+00.4933	1.13	1.30
G330.2935-00.3946	...	0.38	0.63	1.51
G330.8845-00.3721	1.60	0.85	1.62	1.25	0.40	2.90
G330.9544-00.1817	1.08	0.51	1.00	0.90	0.38	2.07
G331.1282-00.2436	2.11	0.42	0.66	0.79	...	1.33
G331.4181-00.3546	2.55	2.01

Table 3—Continued

RMS name	N ₂ H ⁺ Group2 (K)	C ₂ H F = 1 - 0 (K)	C ₂ H F = 2 - 1 (K)	HC ₃ N J = 10 - 9 (K)	HN ¹³ C J = 1 - 0 (K)	HNC J = 1 - 0 (K)
G331.5582-00.1206	2.43	0.55	...	1.87
G332.1544-00.4487	0.71	0.39	0.78	1.49
G332.2944-00.0962	2.85	0.63	1.15	0.77	...	2.20
G332.8256-00.5498	2.68	0.74	1.30	1.48	0.58	3.26
G333.0299-00.0645	0.85	0.46	1.00	0.65	...	1.13
G333.0494+00.0324	1.00	0.43	0.80	1.74
G333.1642-00.0994	1.61	0.72
G336.3684-00.0033	...	0.24	0.68	2.54
G337.0047+00.3226	0.92	1.17
G337.4050-00.4071	2.76	0.86	1.65	1.82	0.54	3.87
G337.8442-00.3748	2.00	0.52	0.98	1.00	...	2.29
G337.9947+00.0770	...	0.50	0.83	2.21
G338.0715+00.0126	1.03
G339.1052+00.1490	1.59	1.35
G340.0708+00.9267	1.73	0.45	0.90	0.52	...	2.40
G340.2480-00.3725	5.88	0.67	1.10	1.60	0.96	3.41
G342.7057+00.1260	3.01	0.87	1.45	1.74	0.70	3.55
G344.4257+00.0451	2.06	0.55	0.92	0.96	0.47	2.13
G345.0034-00.2240	2.64	0.30	0.61	1.36	0.59	1.09
G345.4881+00.3148	4.10	1.15	2.29	1.95	0.65	5.15
G345.6495+00.0084	0.57
G346.0774-00.0562	1.99	1.22
G346.5235+00.0839	0.70
G347.8707+00.0146	0.92	0.37	0.64	1.34
G348.8922-00.1787	0.68	0.22	0.44	1.18
MYSOs						
G305.2017+00.2072	...	0.41	1.03	0.96	...	2.86
G310.0135+00.3892	1.90	0.52	1.31	0.88	...	2.78
G313.7654-00.8620	3.92	0.49	0.91	0.90	0.62	3.42
G314.3197+00.1125	1.99	0.42	...	0.75
G318.9480-00.1969	4.17	0.53	1.05	1.24	0.53	2.72
G320.2437-00.5619	0.97	0.59
G326.4755+00.6947	4.83	0.49	1.20	1.23	0.59	2.68
G326.5437+00.1684	2.00	0.43	0.52	1.83

Table 3—Continued

RMS name	N ₂ H ⁺ Group2 (K)	C ₂ H F = 1 - 0 (K)	C ₂ H F = 2 - 1 (K)	HC ₃ N J = 10 - 9 (K)	HN ¹³ C J = 1 - 0 (K)	HNC J = 1 - 0 (K)
G327.1192+00.5103	1.03	0.34	0.50	0.69
G329.0663-00.3081	2.40	0.38	0.55	0.73	0.47	2.26
G330.9288-00.4070	1.92	0.52	0.72	0.43	0.49	1.91
G332.4683-00.5228	3.21	0.62	1.04	1.04	0.58	2.45
G332.9636-00.6800	3.18	0.44	0.99	1.29	...	1.78
G333.3151+00.1053	3.63	0.54	0.76	0.94	0.50	3.13
G333.3752-00.2015	0.79	0.94
G335.0611-00.4261	2.78	1.60
G337.1555-00.3951
G338.2801+00.5419	2.16	2.71
G338.9196+00.5495	5.14	0.53	0.91	1.25	0.61	3.41
G339.6221-00.1209	3.39	0.43	0.48	0.84	0.61	2.52
G341.1281-00.3466	1.63	2.33
G341.2182-00.2136	3.97	0.44	1.08	0.88	...	2.33
G342.9583-00.3180	1.68	1.77
G343.5213-00.5171	2.66	0.60	...	1.31
G345.2619-00.4188	1.20	...	0.67	0.51	...	1.20
G345.7172+00.8166	3.41	0.81	1.01	1.22	0.70	2.57
G346.4809+00.1320	0.52	0.77
G348.6491+00.0225	0.80	0.67

Table 4. Column densities of N_2H^+ , C_2H , HC_3N , HNC .

RMS name	N_2H^+ 10^{13} cm^{-2}	C_2H 10^{14} cm^{-2}	HC_3N 10^{13} cm^{-2}	HNC 10^{14} cm^{-2}
HII regions				
G300.5047-00.1745	...	4.37 (0.55)
G301.1364-00.2249	0.73(0.06)	10.51(0.51)	1.77(0.07)	...
G301.8147+00.7808	0.38(0.06)	1.81 (0.36)
G302.0319-00.0613	...	4.57 (0.61)
G302.4867-00.0308
G307.5606-00.5871	1.68(0.08)	4.07 (0.49)	0.84(0.07)	...
G307.6138-00.2559	0.71(0.08)	5.76 (0.40)
G309.9206+00.4790
G310.1420+00.7583	0.96(0.09)	3.26 (0.31)	1.04(0.08)	...
G311.6264+00.2897
G316.1386-00.5009	1.16(0.07)	7.81 (0.59)	0.57(0.05)	...
G317.4298-00.5612
G318.9148-00.1647	0.4 (0.08)	...
G320.7779+00.2412	0.31(0.05)
G321.7209+01.1711	1.23(0.16)	4.67 (0.67)	0.66(0.08)	...
G323.4468+00.0968	0.93(0.05)
G324.1997+00.1192	...	4.01 (0.48)
G326.4477-00.7485	1.32(0.08)	...	0.71(0.07)	...
G326.4719-00.3777	1.46(0.08)	5.49 (0.41)	0.79(0.06)	...
G326.7249+00.6159	2.32(0.11)	6.16 0.48	1.33(0.11)	...
G328.3067+00.4308	...	16.11(0.98)	0.87(0.13)	...
G328.8074+00.6324	1.47(0.13)	9.15 (0.85)	3.21(0.06)	2.83 (0.17)
G328.9580+00.5671	1.05(0.07)	5.65 (0.56)	0.73(0.06)	...
G329.3371+00.1469	1.56(0.1)	9.00 (0.60)	1.39(0.15)	3.28 (0.11)
G329.4055-00.4574	1.34(0.2)	6.03 (0.61)	1.65(0.08)	2.25 (0.20)
G329.4211-00.1631	1.61(0.13)	2.64 (0.36)	0.55(0.06)	...
G329.4761+00.8414	0.41(0.05)
G329.8145+00.1411	1.17(0.07)
G330.2845+00.4933	0.66(0.03)
G330.2935-00.3946	...	3.54 (0.34)
G330.8845-00.3721	1.58(0.1)	10.6 (0.52)	2.62(0.05)	3.54 (0.13)
G330.9544-00.1817	...	9.19 (0.58)	3.31(0.29)	7.60 (0.80)
G331.1282-00.2436	2.48(0.11)	7.04 (0.53)	1.93(0.06)	...
G331.4181-00.3546	1.47(0.31)

Table 4—Continued

RMS name	N ₂ H ⁺ 10 ¹³ cm ⁻²	C ₂ H 10 ¹⁴ cm ⁻²	HC ₃ N 10 ¹³ cm ⁻²	HNC 10 ¹⁴ cm ⁻²
G331.5582-00.1206	1.58(0.07)	...	0.92(0.06)	...
G332.1544-00.4487	...	8.54 (0.54)
G332.2944-00.0962	1.78(0.13)	5.43 (0.57)	1.02(0.05)	...
G332.8256-00.5498	4.01(0.59)	16.66(1.81)	3.98(0.16)	7.89 (0.58)
G333.0299-00.0645	0.55(0.07)	3.91 (0.53)	0.66(0.06)	...
G333.0494+00.0324	0.50(0.04)	3.06 (0.40)
G333.1642-00.0994	1.06(0.13)
G336.3684-00.0033	...	3.16 (0.41)
G337.0047+00.3226	0.7 (0.11)
G337.4050-00.4071	2.28(0.08)	8.57 (0.41)	2.94(0.07)	3.97 (0.07)
G337.8442-00.3748	1.19(0.07)	3.91 (0.37)	0.68(0.05)	...
G337.9947+00.0770	...	4.68 (0.37)
G338.0715+00.0126
G339.1052+00.1490	1.01(0.06)
G340.0708+00.9267	1.29(0.12)	3.47 (0.40)	0.7 (0.07)	...
G340.2480-00.3725	4.24(0.17)	6.36 (0.51)	2.39(0.04)	6.90 (0.47)
G342.7057+00.1260	3.24(0.12)	9.98 (0.56)	2.43(0.04)	4.07 (0.22)
G344.4257+00.0451	1.68(0.07)	7.39 (0.59)	1.04(0.06)	2.94 (0.11)
G345.0034-00.2240	2.42(0.93)	3.86 (1.59)	4.25(0.32)	11.48 (3.64)
G345.4881+00.3148	3.33(0.21)	13.39(0.72)	3.72(0.16)	4.62 (0.21)
G345.6495+00.0084
G346.0774-00.0562	1.34(0.22)
G346.5235+00.0839
G347.8707+00.0146	...	4.44 (0.43)
G348.8922-00.1787	0.58(0.07)	2.34 (0.37)
MYSOs				
G305.2017+00.2072	...	7.74 (0.48)	3.11 (0.11)	...
G310.0135+00.3892	1.91 (0.10)	3.26 (0.26)	0.69 (0.06)	...
G313.7654-00.8620	3.00 (0.24)	4.61 (0.58)	1.55 (0.08)	3.71 (0.23)
G314.3197+00.1125	1.34 (0.08)	...	0.49 (0.06)	...
G318.9480-00.1969	3.22 (0.08)	3.65 (0.24)	1.68 (0.08)	4.61 (0.68)
G320.2437-00.5619	0.47 (0.07)
G326.4755+00.6947	3.21 (0.11)	4.96 (0.37)	1.95 (0.09)	...
G326.5437+00.1684	1.18 (0.23)	5.63 (5.22)

Table 4—Continued

RMS name	N_2H^+ 10^{13} cm^{-2}	C_2H 10^{14} cm^{-2}	HC_3N 10^{13} cm^{-2}	HNC 10^{14} cm^{-2}
G327.1192+00.5103	0.79 (0.06)	4.42 (0.71)
G329.0663-00.3081	2.20 (0.12)	4.66 (0.47)	1.81 (0.07)	2.61 (0.09)
G330.9288-00.4070	1.32 (0.05)	3.15 (0.34)	0.49 (0.07)	1.91 (0.07)
G332.4683-00.5228	1.99 (0.10)	5.79 (0.49)	1.54 (0.06)	3.98 (0.17)
G332.9636-00.6800	4.30 (0.37)	5.52 (0.48)	1.98 (0.18)	...
G333.3151+00.1053	2.54 (0.12)	7.31 (0.89)	1.29 (0.08)	2.79 (0.12)
G333.3752-00.2015	0.44 (0.08)
G335.0611-00.4261	2.05 (0.13)
G337.1555-00.3951
G338.2801+00.5419	1.57 (0.08)
G338.9196+00.5495	7.74 (0.36)	8.45 (0.67)	3.46 (0.07)	5.37 (0.29)
G339.6221-00.1209	2.00 (0.09)	15.04(1.78)	0.97 (0.07)	4.26 (0.31)
G341.1281-00.3466	0.96 (0.05)
G341.2182-00.2136	2.81 (0.05)	3.11 (0.16)	1.19 (0.11)	...
G342.9583-00.3180	1.08 (0.07)
G343.5213-00.5171	1.71 (0.14)	...	0.49 (0.03)	...
G345.2619-00.4188	1.37 (0.07)	1.31 (0.18)	0.34 (0.05)	...
G345.7172+00.8166	2.76 (0.13)	7.69 (0.71)	1.14 (0.04)	3.03 (0.19)
G346.4809+00.1320	0.34 (0.16)
G348.6491+00.0225	2.26 (0.26)

Table 5. Abundances of N_2H^+ , C_2H , HC_3N , HNC .

RMS name	N_2H^+ 10^{-9}	C_2H 10^{-8}	HC_3N 10^{-10}	HNC 10^{-8}
HII regions				
G300.5047-00.1745	...	0.56 (0.10)
G301.1364-00.2249	0.04 (0.01)	0.24 (0.03)	0.40 (0.05)	...
G301.8147+00.7808	0.12 (0.04)	0.58 (0.21)
G302.0319-00.0613	...	1.01 (0.22)
G302.4867-00.0308
G307.5606-00.5871	0.13 (0.01)	0.31 (0.05)	0.63 (0.09)	...
G307.6138-00.2559	0.40 (0.08)	1.01 (0.15)
G309.9206+00.4790
G310.1420+00.7583	0.12 (0.02)	0.32 (0.06)	1.01 (0.16)	...
G311.6264+00.2897
G316.1386-00.5009	0.18 (0.03)	1.07 (0.17)	0.78 (0.13)	...
G317.4298-00.5612
G318.9148-00.1647	0.60 (0.22)	...
G320.7779+00.2412	0.09 (0.03)
G321.7209+01.1711	0.15 (0.04)	0.42 (0.13)	0.60 (0.16)	...
G323.4468+00.0968	0.24 (0.03)
G324.1997+00.1192	...	0.26 (0.06)
G326.4477-00.7485	0.23 (0.03)	...	0.93 (0.17)	...
G326.4719-00.3777	0.19 (0.03)	0.51 (0.08)	0.73 (0.11)	...
G326.7249+00.6159	0.15 (0.02)	0.39 (0.06)	0.85 (0.14)	...
G328.3067+00.4308	...	1.21 (0.17)	0.65 (0.15)	...
G328.8074+00.6324	0.03 (0.01)	0.16 (0.03)	0.55 (0.07)	0.05 (0.01)
G328.9580+00.5671	0.15 (0.02)	0.79 (0.14)	1.02 (0.17)	...
G329.3371+00.1469	0.13 (0.02)	0.72 (0.11)	1.12 (0.21)	0.26 (0.03)
G329.4055-00.4574	0.16 (0.05)	0.40 (0.10)	1.10 (0.21)	0.15 (0.04)
G329.4211-00.1631	0.28 (0.05)	0.40 (0.10)	0.82 (0.18)	...
G329.4761+00.8414	0.21 (0.04)
G329.8145+00.1411	0.23 (0.03)
G330.2845+00.4933	0.14 (0.02)
G330.2935-00.3946	...	0.32 (0.06)
G330.8845-00.3721	0.06 (0.01)	0.27 (0.03)	0.67 (0.06)	0.09 (0.01)
G330.9544-00.1817	...	0.14 (0.02)	0.50 (0.08)	0.11 (0.02)
G331.1282-00.2436	0.08 (0.01)	0.22 (0.03)	0.60 (0.05)	...
G331.4181-00.3546	0.26 (0.09)
G331.5582-00.1206	0.10 (0.01)	...	0.49 (0.07)	...

Table 5—Continued

RMS name	N_2H^+ 10^{-9}	C_2H 10^{-8}	HC_3N 10^{-10}	HNC 10^{-8}
G332.1544-00.4487	...	1.14 (0.13)
G332.2944-00.0962	0.13 (0.02)	0.31 (0.07)	0.58 (0.09)	...
G332.8256-00.5498	0.07 (0.02)	0.27 (0.07)	0.65 (0.12)	0.13 (0.03)
G333.0299-00.0645	0.12 (0.04)	0.85 (0.27)	1.43 (0.38)	...
G333.0494+00.0324	0.13 (0.02)	0.80 (0.19)
G333.1642-00.0994	0.81 (0.22)
G336.3684-00.0033	...	0.20 (0.04)
G337.0047+00.3226	0.14 (0.04)
G337.4050-00.4071	0.07 (0.01)	0.22 (0.02)	0.77 (0.06)	0.10 (0.01)
G337.8442-00.3748	0.19 (0.03)	0.63 (0.11)	1.09 (0.17)	...
G337.9947+00.0770	...	0.80 (0.13)
G338.0715+00.0126
G339.1052+00.1490	0.21 (0.03)
G340.0708+00.9267	0.24 (0.05)	0.58 (0.13)	1.18 (0.24)	...
G340.2480-00.3725	0.33 (0.04)	0.45 (0.07)	1.67 (0.16)	0.48 (0.07)
G342.7057+00.1260	0.23 (0.03)	0.65 (0.09)	1.59 (0.15)	0.27 (0.04)
G344.4257+00.0451	0.22 (0.03)	0.86 (0.14)	1.21 (0.17)	0.34 (0.04)
G345.0034-00.2240	0.11 (0.09)	0.09 (0.08)	1.03 (0.45)	0.28 (0.21)
G345.4881+00.3148	0.10 (0.01)	0.37 (0.05)	1.04 (0.13)	0.13 (0.02)
G345.6495+00.0084
G346.0774-00.0562	0.33 (0.12)
G346.5235+00.0839
G347.8707+00.0146	...	0.61 (0.12)
G348.8922-00.1787	0.10 (0.02)	0.42 (0.11)
MYSOs				
G305.2017+00.2072	...	0.24 (0.03)	0.97 (0.11)	...
G310.0135+00.3892	0.23 (0.03)	0.40 (0.06)	0.84 (0.14)	...
G313.7654-00.8620	0.25 (0.05)	0.39 (0.09)	1.31 (0.20)	0.31 (0.05)
G314.3197+00.1125	0.19 (0.03)	...	0.68 (0.14)	...
G318.9480-00.1969	0.19 (0.02)	0.21 (0.03)	0.98 (0.12)	0.27 (0.06)
G320.2437-00.5619	0.08 (0.02)
G326.4755+00.6947	0.08 (0.01)	0.13 (0.02)	0.51 (0.06)	...
G326.5437+00.1684	0.12 (0.05)	0.56 (0.73)
G327.1192+00.5103	0.10 (0.02)	0.56 (0.14)
G329.0663-00.3081	0.17 (0.02)	0.36 (0.07)	1.39 (0.16)	0.20 (0.02)

Table 5—Continued

RMS name	N_2H^+ 10^{-9}	C_2H 10^{-8}	HC_3N 10^{-10}	HNC 10^{-8}
G330.9288-00.4070	0.14 (0.02)	0.34 (0.07)	0.53 (0.12)	0.21 (0.02)
G332.4683-00.5228	0.22 (0.03)	0.63 (0.10)	1.67 (0.20)	0.43 (0.05)
G332.9636-00.6800	0.20 (0.03)	0.26 (0.04)	0.92 (0.16)	
G333.3151+00.1053	0.27 (0.04)	0.78 (0.18)	1.37 (0.23)	0.30 (0.04)
G333.3752-00.2015	0.09 (0.03)
G335.0611-00.4261	0.14 (0.02)
G337.1555-00.3951
G338.2801+00.5419	0.22 (0.03)
G338.9196+00.5495	0.13 (0.02)	0.15 (0.02)	0.59 (0.06)	0.09 (0.01)
G339.6221-00.1209	0.26 (0.03)	1.96 (0.40)	1.27 (0.19)	0.56 (0.09)
G341.1281-00.3466	0.14 (0.02)
G341.2182-00.2136	0.22 (0.01)	0.24 (0.03)	0.94 (0.14)	...
G342.9583-00.3180	0.31 (0.04)
G343.5213-00.5171	0.26 (0.06)	...	0.75 (0.15)	...
G345.2619-00.4188	0.30 (0.03)	0.28 (0.05)	0.74 (0.15)	...
G345.7172+00.8166	0.24 (0.03)	0.66 (0.12)	0.98 (0.11)	0.26 (0.04)
G346.4809+00.1320	0.12 (0.08)
G348.6491+00.0225B	0.46 (0.10)

Table 6: Average column densities and molecular abundances compared with other works.

Different works	Type	N_2H^+	C_2H	HC_3N	HNC
Column Densities (cm^{-2})					
This work	RMSs	1.5×10^{13}	6.4×10^{14}	1.6×10^{13}	4.4×10^{14}
Sanhueza et al. (2012)	IRDCs	1.6×10^{13}	2.4×10^{14}	4.8×10^{13}	2.4×10^{14}
Yu et al. (2015)	EGOs	6.5×10^{13}	5.7×10^{14}
Chen et al. (2013)	EGOs	3.0×10^{13}	...	3.2×10^{13}	...
Molecular Abundances					
This work	RMSs	0.2×10^{-9}	0.5×10^{-8}	0.9×10^{-10}	0.2×10^{-8}
Vasyunina et al. (2011)	IRDCs	2.8×10^{-9}	1.4×10^{-8}	5.4×10^{-10}	0.2×10^{-8}
Sanhueza et al. (2012)	IRDCs	2.4×10^{-9}	3.7×10^{-8}	4.2×10^{-10}	3.7×10^{-8}

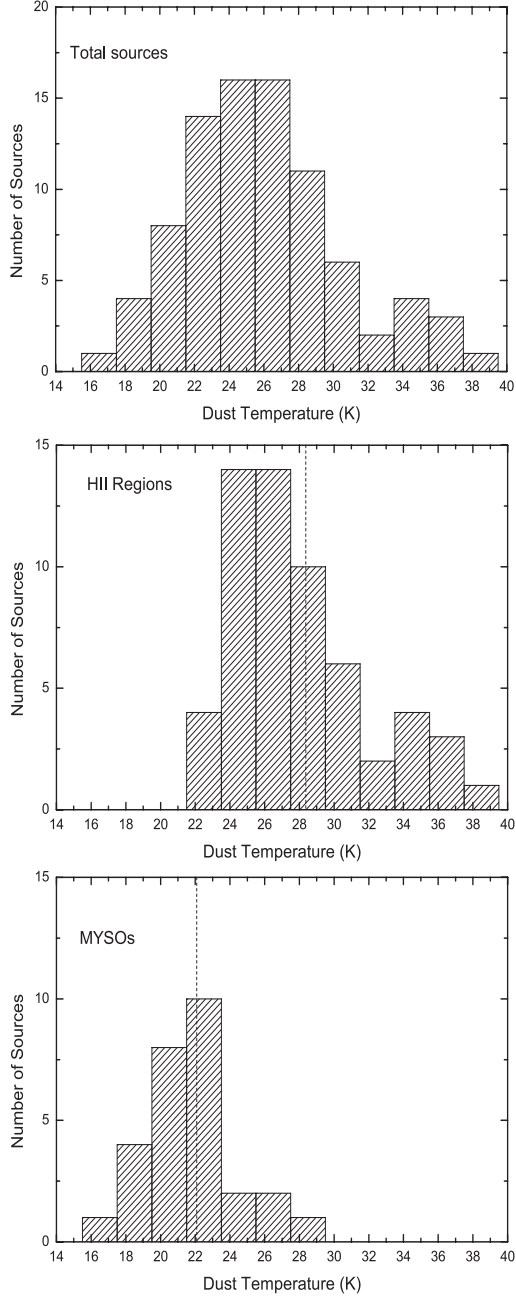


Fig. 1.— Dust temperature distributions of total sources (top), HII regions (middle) and MYSOs (bottom). The dashed vertical lines indicate their mean temperatures.

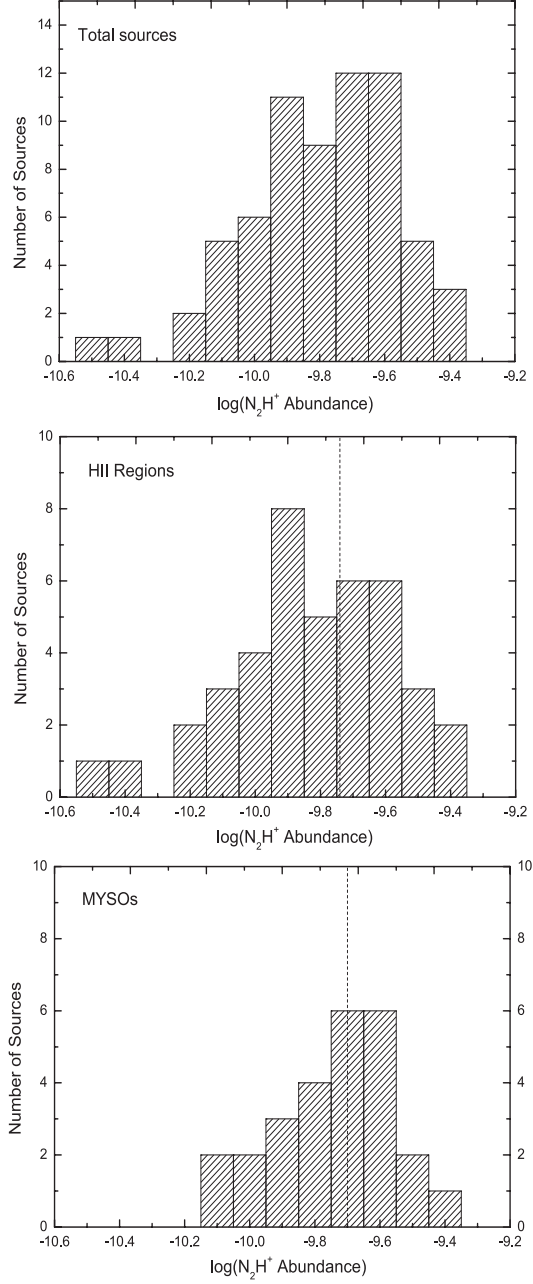


Fig. 2.— Histograms of the number distributions of N_2H^+ abundances for our total RMSs (top), MYSOs (middle) and HII regions (bottom). The dashed lines indicate mean values.

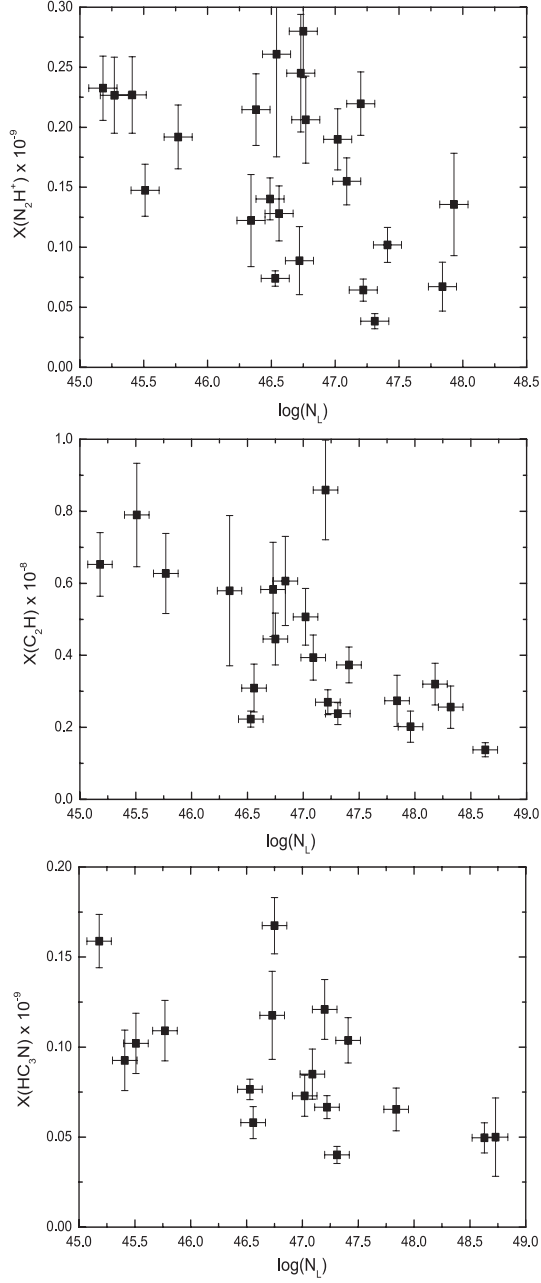


Fig. 3.— Fractional abundances of N_2H^+ (top), C_2H (middle) and HC_3N (bottom) plotted as a function of N_L in logarithmic scales.

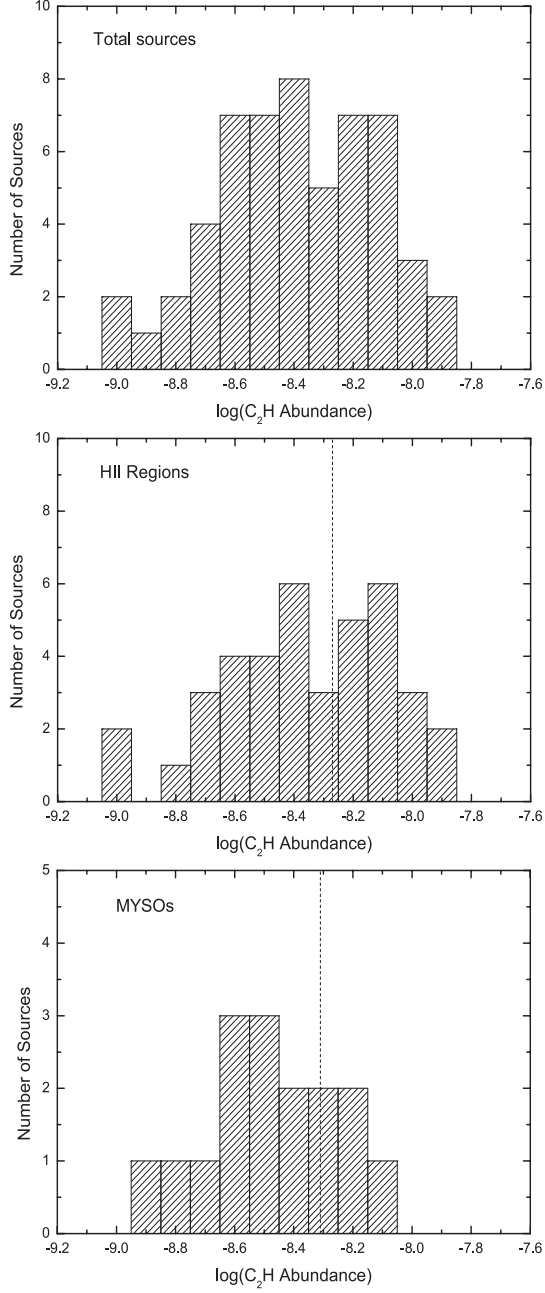


Fig. 4.— Histograms of the number distributions of C₂H abundances for our total RMSs (top), HII regions (middle) and MYSOs (bottom). The dashed lines indicate mean values.

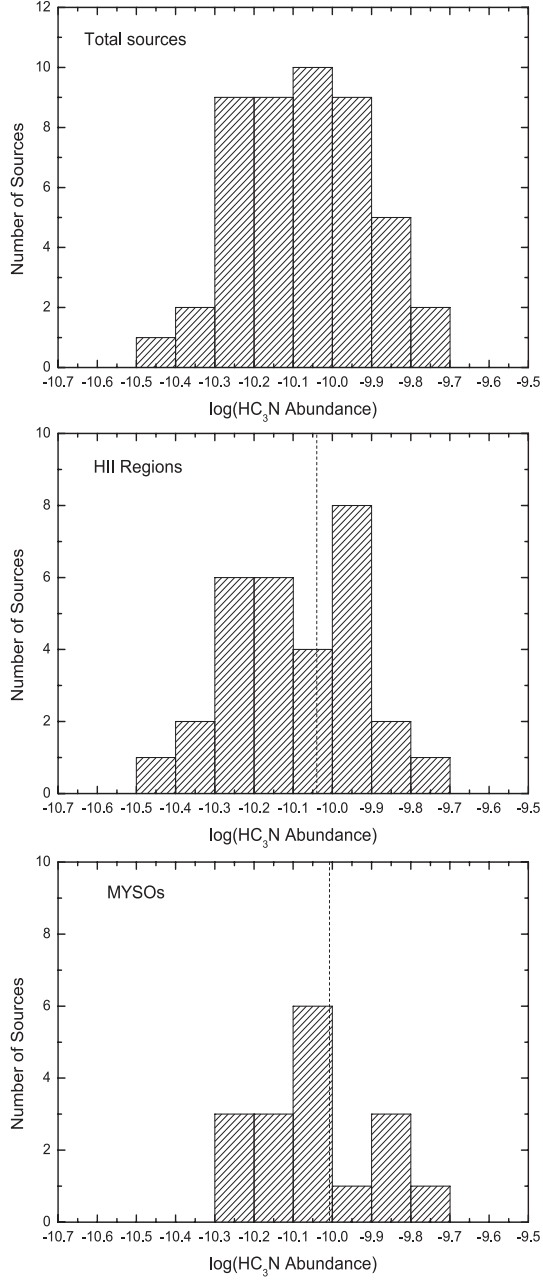


Fig. 5.— Histograms of the number distributions of HC_3N abundances for our total RMSs (top), HII regions (middle) and MYSOs (bottom). The dashed lines indicate mean values.

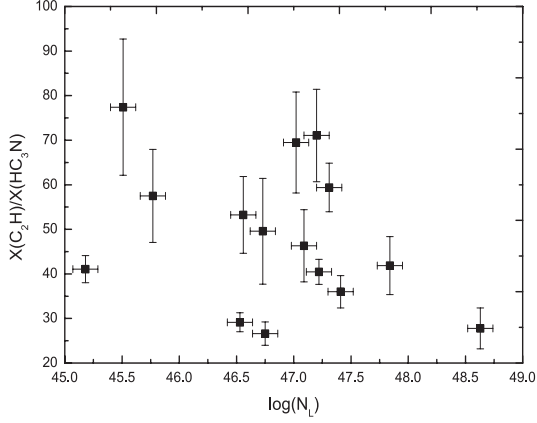


Fig. 6.— The $[C_2H]/[HC_3N]$ relative abundance ratio plotted as a function of N_L in logarithmic scales.

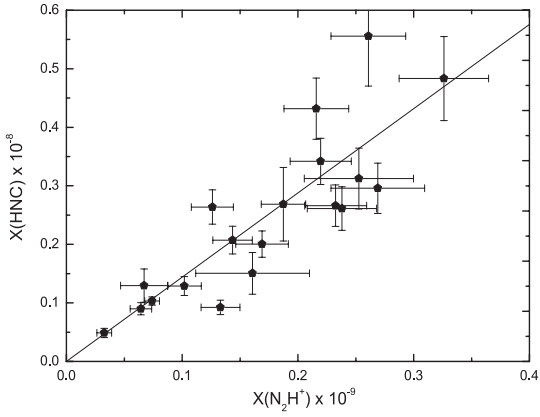


Fig. 7.— HNC fractional abundance plotted as a function of N_2H^+ abundance. The solid line shows the least square fit to the data.